nature communications

Article

https://doi.org/10.1038/s41467-025-59315-y

Overcoming lattice mismatch for core-shell $NaGdF_4$@$CsPbBr_3$ heterostructures

Received: 3 January 2024

Accepted: 17 April 2025

Zhongzheng Yu[1,2,5], Wen Kiat Chan[1,5], Donglei Zhou[3], Xinjuan Li[4], Yang Lu[2], Zhao Jiang[2], Bofeng Xue[2], Huangtianzhi Zhu[2], Simon Dowland[2], Junzhi Ye[2], Alasdair Tew[2], Lars van Turnhout[2], Qichun Gu[2], Linjie Dai[2], Tianjun Liu[2], Caterina Ducati[4], Akshay Rao[2] & Timothy Thatt Yang Tan[1]

The formation of core-shell heterostructures allows direct contact of two components for more efficient energy transfer while requires exquisite lattice match. Lattice mismatch is one of the most challenging obstacles for combining two components with different phases. In this work, we develop a strategy to overcome the limitation of lattice mismatch and grow α-phase lead halide perovskites (LHPs) onto β-phase lanthanide-doped nanoparticles (LnNPs) by seeding sub-8 nm LnNPs. This LnNP@LHP heterostructure effectively passivates the surface defects of LnNPs to obtain enhanced upconversion performance and enables two-way energy transfer within the heterostructures. We identify and prove that core size along with a high reaction temperature, instead of phase, is critical to overcome the lattice mismatch. Our strategy uncovers insights into the key factor of direct growth for heterostructures and we believe the current synthesis strategy for high-quality heterostructures will have strong application potential in optoelectronics, anticounterfeiting and light detection.

The combination of lead halide perovskites (LHPs) and upconversion lanthanide-doped nanoparticles (LnNPs) has attracted great interest in recent years due to their complementary absorption spectra and shown huge potential in broadband light detection, multichannel anticounterfeiting and enhancement of photovoltaic efficiency, etc.[1–8]. LHPs possess broad absorption in the ultraviolet (UV) and entire visible (Vis) range but has limited absorption in the near infrared (NIR) range, while LnNPs can absorb NIR light at different wavelengths by doping different Ln ions but have weak UV and Vis absorption[8–12]. Therefore, the combination of LHPs and LnNPs for heterostructure is highly favorable, promising multiple energy transfer pathways arising from the different combinations.

The fabrication of heterostructures is desirable as this method combines two or more distinct materials to largely enhance the performance of the heterostructures or remedy the limitations of individual components[13]. The core-shell heterostructures allows direct contact for efficient energy transfer and requires exquisite lattice match[14–18]. Thus, lattice mismatch stands as a significant hurdle for the synthesis of heterostructures. This challenge still exists for the fabrication of core-shell LnNP@LHP heterostructures and explains why LnNP@LHP heterostructures have been rarely reported. Compared with Ln^{3+} ion doped systems, heterostructures can provide two-way energy transfer to realize upconversion process with good alignment of energy levels between two components. Moreover, heterostructures can overcome the maximum doping ratio of Ln^{3+} ions into LHP NCs (normally <10%)[19,20]. LHP is well-known for their high defect tolerance property[21], thus can be a good passivation shell to enhance the upconversion performance of small (<10 nm) LnNPs.

Up to date, many approaches have been attempted to combine LHPs and LnNPs. The first approach is physical mixing. This method

---

[1]School of Chemistry, Chemical Engineering and Biotechnology, Nanyang Technological University, Singapore, Singapore. [2]Cavendish Laboratory, University of Cambridge, Cambridge, United Kingdom. [3]State Key Laboratory of Integrated Optoelectronics, College of Electronic Science and Engineering, Jilin University, Changchun, China. [4]Department of Materials Science and Metallurgy, University of Cambridge, Cambridge, United Kingdom. [5]These authors contributed equally: Zhongzheng Yu, Wen Kiat Chan. e-mail: yuzh0010@e.ntu.edu.sg; tytan@ntu.edu.sg

is simple but the distance between LHPs and LnNPs is not fixed, and thus their energy transfer is based on emission reabsorption with low efficiency. Guo et al. synthesized LnNPs which were then mixed into a TiO_2 mesoporous layer[22]. The second approach is the usage of an intermediate 'glue' to combine LnNPs and LHPs. Francés-Soriano et al. used cucurbit[7]uril to anchor $CH_3NH_3PbBr_3$ LHPs onto LnNPs and reported energy transfer under NIR excitation between the LnNP donors and LHP acceptors via the lanthanide resonance energy transfer (LRET) pathway due to the 1 nm distance between the components[23]. Additionally, block copolymers[24] and mesoporous silica[25] were also applied to mediate the co-assembly of LHPs and LnNPs. This approach can achieve higher energy transfer efficiencies but need specific and expensive linker groups. The third approach is by forming superlattices. Kovalenko's group reported perovskite-type superlattices by combining LHPs and LnNPs using shorter tail ligands[26], which requires ligand exchange and only applicable to thin films. The fourth method is forming core-shell heterostructures. This method enables direct contact of two components with more efficient energy transfer. These recently reported heterostructures still require lattice matching between LHPs and LnNPs, with both components being in the same cubic (α) phase[16]. Zhang's group achieved watermelon-like mix-phase heterostructures, with α-phase LHPs as watermelon seeds and hexagonal (β)-phase upconversion LnNPs as watermelon pulp and skin. This heterostructures grew from α-phase upconversion LnNPs and then underwent phase transition to β-phase due to heat treatment[15].

Thus far, the synthesis of LHP-LnNP heterostructures has been limited to phase and lattice matches. In this work, we provide a strategy to achieve direct growth of LnNP@LHP heterostructures by seeding small LnNPs in the growth of $CsPbBr_3$ LHPs, regardless of crystal phase of LnNP cores. Furthermore, we proved that size, rather than the crystal phase of LnNPs plays a more important role in the fabrication of LnNP@LHP heterostructures. By embedding LnNPs into LHPs, we can achieve a higher defect tolerance by using LHPs to passivate the surface defects of LnNPs. Two-way energy transfer is demonstrated for the α/β-LnNP@$CsPbBr_3$ heterostructures, as a 980 nm $CsPbBr_3$-sensitized Yb^{3+} emission was obtained using 365 nm excitation, while under 980 nm excitation, a green lanthanide-sensitized $CsPbBr_3$ emission was observed. As a result, this heterostructure involving LnNP as core and LHP as shell has strong application potential in optoelectronics, anticounterfeiting and X-ray/NIR light detection. Our method of seeding small LnNPs as cores will also contribute to the development of different heterostructures with enhanced optical performance.

Results and discussion

Core-shell heterostructures using α-phase LnNPs and LHPs

Optically inert α-phase $NaYF_4$ LnNPs were synthesized using a modified co-precipitation technique (Supplementary Figs. 1, 2)[27–29]. The reduced amount of NaF precursor and shortened reaction time result in uniform α-$NaYF_4$ LnNPs with an average size of 4.9 ± 0.4 nm. The as-prepared LnNPs were used to seed the growth of $CsPbX_3$ (X=Cl, Br, I) nanocrystals (NCs). The cubic phase LHPs have the same lattice angles $\alpha = \beta = \gamma = 90°$, with different lattice lengths $a = b = c = 5.68$ Å for $CsPbCl_3$, 5.95 Å for $CsPbBr_3$, and 6.28 Å for $CsPbI_3$, respectively. α-$NaYF_4$ NCs also have the same angle constants with a length parameter of 5.52 Å. This provides the possibility to form α-$NaYF_4$@$CsPbX_3$ heterostructures. We found that we could only form α-$NaYF_4$@$CsPbCl_3$/Br_3 heterostructures, the combination of α-$NaYF_4$ + $CsPbI_3$ formed nanowire superstructures (NWSSs) (Supplementary Fig. 1). We attributed the formation of NWSSs using $CsPbI_3$ instead of heterostructures to the larger ionic radius of I^- compared with the ionic radii of Br^- and Cl^-. The tolerance factor of $CsPbI_3$ is 0.81, which approaches the lower limit of tolerance factor to remain stable (the range of 0.8–1.11)[30,31]. Thus, $CsPbI_3$ cannot coat on the surface of LnNPs.

The transmission electron microscopy (TEM) images of α-$NaYF_4$@$CsPbCl_3$/Br_3, high-resolution TEM (HRTEM) lattice distances and XRD patterns show characteristic cubic phase features (Supplementary Figs. 1, 2), similar to that obtained by pristine $CsPbX_3$ NCs synthesized via hot injection (Supplementary Fig. 3)[32,33]. XRD patterns of these heterostructures show a combination of diffraction peaks of both cubic-phase $NaYF_4$ and $CsPbCl_3$/Br_3 (Supplementary Fig. 2)[34,35].

Subsequently, we measured the emission spectra of the α-$NaYF_4$@$CsPbCl_3$/Br_3 heterostructures to study the fluorescence change of LHP shells. Perovskite NCs are known to interact with one another, leading to concentration dependent red shifted emission due to either the interdot effect or reabsorption at high concentrations[36–41]. When perovskite samples are continually diluted, the emission peaks continuously blue shift until a terminal point which reflects the emission of individual NC is reached, which we term the emission convergence point (ECP)[40,42]. The ECP therefore, allows comparison for different samples. The formation of α-$NaYF_4$@$CsPbCl_3$/Br_3 core-shell structures leads to a smaller effective $CsPbCl_3$/Br_3 shell size compared to that of pure $CsPbCl_3$/Br_3 NCs and this may affect the ECP values of the heterostructures depending on the exciton Bohr radius of $CsPbCl_3$/Br_3. The ECP values of α-$NaYF_4$@$CsPbCl_3$ and $CsPbCl_3$ are both at 403 nm with no observed quantum confinement effect due to the small exciton Bohr radius of $CsPbCl_3$ of ≈3 nm (Supplementary Fig. 4)[43]. The ECP of α-$NaYF_4$@$CsPbBr_3$ is blue-shifted by 4 nm compared to pure $CsPbBr_3$, due to the 4.9 nm LnNPs embedded within α-$NaYF_4$@$CsPbBr_3$ heterostructures with an average size of 10.4 ± 1.5 nm, giving rise to an effective $CsPbBr_3$ size smaller than that of the $CsPbBr_3$ exciton Bohr radius of 7 nm (Supplementary Fig. 4)[44]. We have grown $CsPbCl_3$/Br_3 onto sub-5 nm α-$NaYF_4$, forming α-LnNP@α-LHP heterostructures using the two components with the same phase as expected. In the case of $CsPbI_3$, α-$NaYF_4$ + $CsPbI_3$ NWSSs were formed, implying that the halide group influences crystal growth and that LnNPs can mediate the assembly or structure of LHPs.

Combining optically inert β-LnNPs with LHPs

The key barrier in fabricating heterostructures is lattice mismatch, which can be overcome by always requiring a close lattice parameter or at least a similar phase. The as-synthesized α-phase LnNPs have a small lattice mismatch compared to α-phase $CsPbCl_3$/Br_3, and could be surmounted[15]. We now try to overcome the barrier of lattice mismatch using small β-phase LnNPs to seed the growth of α-LHPs, which have bigger lattice mismatch and even different phases. This will give us deeper insights into the growth mechanism of LHP onto LnNPs. The lattice constants of β-$NaGdF_4$ are $a = 6.02$ Å, $c = 3.60$ Å, $\alpha = \beta = 90°$, $\gamma = 120°$[45]. β-$NaGdF_4$ LnNPs have lowest energy levels of ≈4 eV, so can be deemed as optically inert. The as-synthesized optically inert β-LnNP core will provide key structural evidence for the formation of mixed phase heterostructures, allowing us to focus on the energy transfer using optically active LnNP cores.

We started by synthesizing small β-$NaGdF_4$ using a modified method and studied the morphology using TEM. TEM images reveal nanoparticles with an average size of 3.7 ± 0.3 nm (Fig. 1a and Supplementary Fig. 5), while XRD patterns (PDF #27-0699) match that of hexagonal phase $NaGdF_4$ with a broadened diffraction peak indicating weak crystallinity (Supplementary Fig. 6). The small β-$NaGdF_4$ LnNPs are then used to seed the growth of $CsPbBr_3$, and the resulting sample is denoted as β-$NaGdF_4$@$CsPbBr_3$ heterostructures. High-angle annular dark-field scanning transmission electron microscopy (HAADF-STEM) images showed clear and uniform core-shell heterostructures with an average size of 9.5 ± 0.1 nm (Fig. 1b and Supplementary Fig. 5). Some heterostructures have multiple LnNP cores, and a small portion of LnNPs is not coated. This could be solved by tuning the mass ratio of core LnNPs and perovskite precursors. HAADF-STEM image contrast is related to the elastic scattering of electrons in the sample[46], thus different types of nanomaterials could be identified by measuring the

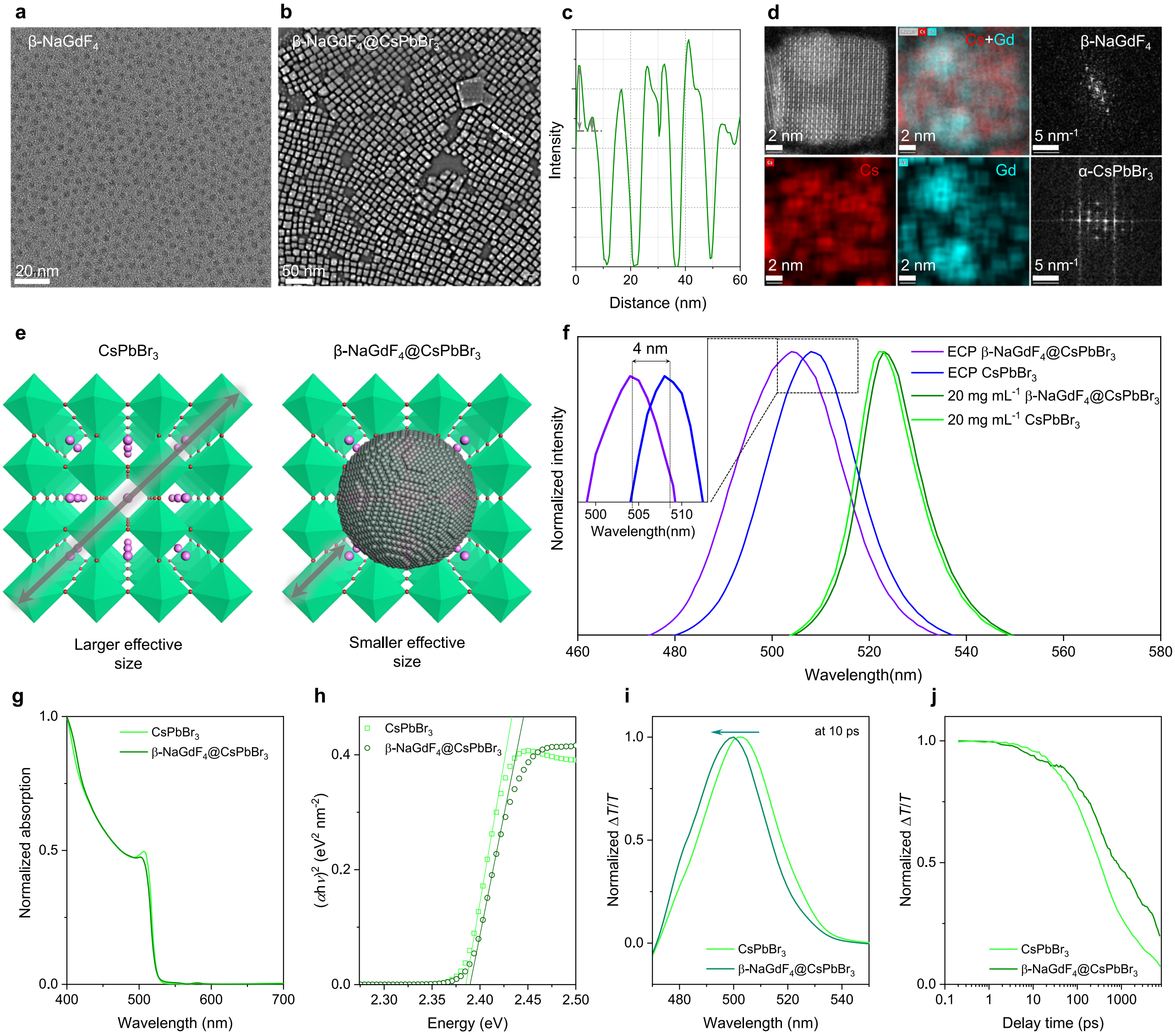

Fig. 1 | Fabrication of optically inert β-NaGdF$_4$@CsPbBr$_3$ heterostructures. **a** TEM image of β-NaGdF$_4$ LnNPs. **b** HAADF-STEM image of β-NaGdF$_4$@CsPbBr$_3$ heterostructures. **c** Corrected HAADF line profile to show the intensity variations along the white line. **d** EDS elemental mapping of a single β-NaGdF$_4$@CsPbBr$_3$ heterostructure along with the diffraction pattern of β-phase NaGdF$_4$ and α-phase CsPbBr$_3$. **e** Schematic illustration of CsPbBr$_3$ NC and β-NaGdF$_4$@CsPbBr$_3$ heterostructure and their effective sizes. **f** Emission spectra of β-NaGdF$_4$@CsPbBr$_3$ heterostructures with inset emphasizing blue shift in β-NaGdF$_4$@CsPbBr$_3$ heterostructure emission compared to pure CsPbBr$_3$. Samples were excited using 365 nm lamp and dispersed in hexane. **g** Absorption spectra and **h** Tauc plot of CsPbBr$_3$ and β-NaGdF$_4$@CsPbBr$_3$. **i** Transient absorption spectra at 10 ps, and **j** GSB kinetics at a fluence of 6.1 μJ cm^{-2} of CsPbBr$_3$ NCs and β-NaGdF$_4$@CsPbBr$_3$ heterostructures under 400 nm pump. Source data are provided as a Source Data file.

intensities of HAADF-STEM images (see Supplementary Note 1). According to the corrected line scanning profile (white line in Fig. 1b) of five heterostructures, we could conclude that more than one LnNP could be seeded in the heterostructures, confirming the fabrication of core-shell heterostructures (Fig. 1c, see Supplementary Note 1). We further used HAADF-STEM to analyze a single heterostructure (Fig. 1d). The energy-dispersive X-ray spectroscopy (EDS) elemental mapping of a single heterostructure clearly showed 2 β-NaGdF$_4$ cores embedded within the CsPbBr$_3$ shell.

XRD patterns of β-NaGdF$_4$@CsPbBr$_3$ heterostructures showed a combination of cubic phase CsPbBr$_3$ peaks and hexagonal phase β-NaGdF$_4$, identified by the characteristic (100) peak of β-NaGdF$_4$ (Supplementary Fig. 6)[35]. We next studied the emission spectra of β-NaGdF$_4$@CsPbBr$_3$ under 365 nm excitation to observe any changes compared to pure CsPbBr$_3$ by comparing the ECPs of the samples. The ECP of β-NaGdF$_4$@CsPbBr$_3$ (504 nm) was once again blue shifted by 4 nm compared to pure CsPbBr$_3$ (508 nm) and consistent with that of α-NaYF$_4$@CsPbBr$_3$, supporting our explanation of quantum confined emission (Fig. 1e, f). Figure 1g shows the absorption spectra of pure CsPbBr$_3$ NCs and β-NaGdF$_4$@CsPbBr$_3$ heterostructures. The Tauc plot showed a blue shift of 5 meV of the bandgap of CsPbBr$_3$ after forming the heterostructures (Fig. 1h). The transient absorption spectra at 10 ps of β-NaGdF$_4$@CsPbBr$_3$ heterostructures showed a blue shift of 2 nm (Fig. 1i). The kinetics of CsPbBr$_3$ at its ground state bleach (GSB) (Fig. 1j), which corresponds to the band-filling effect at the band edge, proved that β-NaGdF$_4$@CsPbBr$_3$ heterostructures would lead to a longer lifetime of 4.1 ns compared to that of CsPbBr$_3$ (1.2 ns) at a low fluence of 6.1 μJ cm^{-2}. This suggests that the CsPbBr$_3$ shell in heterostructures have fewer defects due to the high reaction temperature. At higher fluences, the lifetimes of both decrease due to Auger recombination. They are almost identical when fluence is larger than 12.2 μJ cm^{-2} (Supplementary Fig. 7). These data proved that the presence of optically inert β-NaGdF$_4$ would not significantly quench the fluorescence of CsPbBr$_3$.

Small LnNPs could accommodate thicker LHP shells without the formation of strain-relaxing crystalline defects, as the interfacial stress which arises from growing a lattice-mismatched shell could be distributed on the structurally flexible LHP shell[17,47–50]. Apart from this, small LnNPs tend to have poorer crystallinity which reduces the interfacial strain associated with lattice mismatch, compared to larger LnNPs (>10 nm) with improved crystallinity[17,51]. To summarize, the formation of β-$NaGdF_4$@$CsPbBr_3$ heterostructures has been achieved despite the significant lattice mismatch of the individual components.

Two-way energy transfer in heterostructures

α-phase LnNPs are known for their weaker emission compared to β-phase LnNPs[52–55]. Thus, β-phase LnNP cores could result in higher upconversion intensities compared to α-phase cores even with the same surface passivation. We now extend our investigation into optically active, cubic/hexagonal phase LnNPs to study the possibility of energy transfer and surface defect passivation within LnNP@LHP core-shell heterostructures. The performances of the two-way energy transfer between α/β-LnNPs and $CsPbBr_3$ were measured and compared. α-$NaY_{0.69}F_4$:$Yb_{0.3}$,$Tm_{0.01}$ (α-LnNP) and β-$NaGd_{0.69}F_4$:$Yb_{0.3}$,$Tm_{0.01}$ (β-LnNP) were synthesized using the same modified co-precipitation technique and characterized. TEM images show the α-LnNPs with an average size of 7.2 ± 0.7 nm, and β-LnNPs with an average size of 7.1 ± 0.4 nm (Supplementary Fig. 8). XRD patterns further confirm that α-phase and β-phase of these LnNPs (Supplementary Fig. 9). Both optically active α/β-LnNPs absorb light in the NIR region and generate blue emissions under 980 nm excitation (Supplementary Fig. 10). These small LnNPs show relatively poor upconversion performance due to a huge portion of surface defects, which is a key bottleneck to the advancement of LnNP field[27].

We then use α-LnNPs and β-LnNPs as seeds for the growth of $CsPbBr_3$ via hot injection to form heterostructures which we now denote as α-LnNP@$CsPbBr_3$ and β-LnNP@$CsPbBr_3$. The synthesized samples were characterized using HAADF-STEM, which revealed heterostructures of sizes 14.3 ± 2.0 and 16.7 ± 2.0 nm respectively (Fig. 2a, Supplementary Fig. 8). Furthermore, we can directly observe the coating process of $CsPbBr_3$ wrapping on a β-LnNP core in the HAADF-STEM measurement (Fig. 2a) and the corresponding EDS elemental mapping and phase analysis of β-LnNP core and α-$CsPbBr_3$ shell (Fig. 2b). The HAADF-STEM image and corresponding EDS elemental mapping of a single heterostructure further proves the existence and location of β-LnNP cores (Supplementary Fig. 11). XRD patterns of α-LnNP@$CsPbBr_3$ and β-LnNP@$CsPbBr_3$ heterostructures show combinations of diffraction peaks from α/β-LnNPs and $CsPbBr_3$ (Supplementary Fig. 9). The (110) and (200) peaks of LHP in β-LnNP@$CsPbBr_3$ heterostructures shift to higher angles, indicating a reduction in the lattice spacing (*d*-spacing) of LHP shell following Bragg's law $n\lambda=2d\sin\theta$. Thus, seeding the β-LnNP cores with lattice mismatch will compress the $CsPbBr_3$ shell lattice. $CsPbBr_3$ has the structural flexibility to tolerate compressed strain.

The optical properties of α/β-LnNP@$CsPbBr_3$ are now investigated under 365 and 980 nm excitation. Using 365 nm excitation, we found two main peaks, in which the first corresponds to the emission of $CsPbBr_3$. The second peak under 365 nm excitation matches that of Yb^{3+} ions at 980 nm (Fig. 2c), with the emission of the β-LnNP@$CsPbBr_3$ heterostructures being 1.6-fold higher than the α-LnNP@$CsPbBr_3$ heterostructures at the same weight mass. The NIR photoluminescence quantum efficiency (PLQE) of Yb^{3+} in β-LnNP@$CsPbBr_3$ heterostructures is measured to be 2-fold higher than that of α-LnNP@$CsPbBr_3$ heterostructures (Supplementary Table 1). Given that α/β-LnNPs cannot be activated by 365 nm light and the absorption of α/β-LnNP@$CsPbBr_3$ heterostructures is dominated by $CsPbBr_3$, we hereby propose that $CsPbBr_3$ absorbs UV light and transfers energy to Yb^{3+} ions to emit at 980 nm via the defect states (Fig. 2h), which is also reported in the Ln-doped LHP systems for quantum cutting[7]. The RETU mechanism from $CsPbBr_3$ to Yb^{3+} is not possible as the emission of $CsPbBr_3$ is at around 520-530 nm and cannot be absorbed by Tm^{3+} or Yb^{3+} ions. Figure 2d shows the TA kinetics of $CsPbBr_3$ at its GSB before and after shelling. The lifetimes have been shortened from 2.9 to 1.5 to 1.3 ns for $CsPbBr_3$, α-LnNP@$CsPbBr_3$, and β-LnNP@$CsPbBr_3$, respectively, at relatively high fluence of 23.1 μJ cm^{-2}. The shortening of lifetime of $CsPbBr_3$ in the heterostructures can be used to evaluate the energy transfer efficiency (η)[56]. This proves that β-LnNP@$CsPbBr_3$ heterostructures have a higher η to obtain NIR downconversion than α-LnNP@$CsPbBr_3$ heterostructures, further supporting the proposed defect state mediated energy transfer within these heterostructures.

In the case of 980 nm excitation, we found that both α- and β-LnNP@$CsPbBr_3$ heterostructures could generate green emission from $CsPbBr_3$ (Fig. 2e). The β-LnNP@$CsPbBr_3$ heterostructures showed a more efficient upconversion efficiency as the PLQE of β-LnNP@$CsPbBr_3$ heterostructures is 6-fold higher than α-LnNP@$CsPbBr_3$ heterostructures (Supplementary Table 1). Since only Yb^{3+} ions absorb 980 nm light, Yb^{3+}ions act as the sensitizers, and energy is then transferred to Tm^{3+} ions via the energy transfer upconversion (ETU) mechanism. These Tm^{3+} ions then transfer energy to $CsPbBr_3$ by the non-radiative LRET pathway (Fig. 2i), resulting in the green $CsPbBr_3$ emission[24].

Compared to the direct physical mixing of β-LnNPs and $CsPbBr_3$ NCs, the fabrication of heterostructures significantly improve the upconversion performance and energy transfer efficiency under 980 nm excitation. We normalized the emission of the β-LnNPs and the corresponding mixtures or heterostructures by the 646 nm emission ($^1G_4 \rightarrow {}^3F_4$) from Tm^{3+} ions, which is not influenced by the emission reabsorption of $CsPbBr_3$. We find the formation of heterostructures reacted at 220 °C will lead to a more than 10-fold enhancement of the upconversion intensity and main emission color from blue to green, compared to a 1.9-fold enhancement reacted at 210 °C and a 0.4-fold decrease when physically mixed (Fig. 2f, g and Supplementary Fig. 12). This also proves that a high reaction temperature is crucial to help to overcome the lattice mismatch between different components, meanwhile maintaining the α phase of $CsPbBr_3$. We have therefore demonstrated that two-way energy transfer occurs within α/β-LnNP@$CsPbBr_3$ heterostructures, and that $CsPbBr_3$ shelling is proven to enhance the optical performance of LnNPs in upconversion.

The size limit of LnNPs to form heterostructures

It is evident that β-phase LnNPs could be coated by α-phase $CsPbBr_3$ shell. Given the fact that these LnNPs are <10 nm maintaining the β phase, the size of LnNPs clearly plays an important role in the formation of core-shell heterostructures. To further study the effect of core size on the heterostructure growth, we now synthesized optically active β-phase LnNPs in the form of $NaGd_{0.79}F_4$:$Yb_{0.2}$,$Tm_{0.01}$ with larger sizes. LnNP40 and LnNP60 were synthesized by increasing the reaction time to 40 and 60 min, leading to larger average sizes to 7.6 ± 0.8 and 9.2 ± 0.7 nm (Fig. 3a, d, h), respectively. Larger multilayer core-shell-shell (CSS) LnNPs with a configuration of $NaGd_{0.79}F_4$:$Yb_{0.2}Tm_{0.01}$@$NaGd_{0.3}F_4$:$Yb_{0.7}$@$NaGdF_4$ with an average size of 16.7 ± 0.8 nm were also synthesized via epitaxial growth (Supplementary Fig. 13). These larger LnNPs were utilized to seed the growth of $CsPbBr_3$ and explore the size limit to break the lattice mismatch.

Figure 3b shows that only some of the smaller LnNP40 NPs could be seeded in $CsPbBr_3$ NCs, while the larger LnNP40 NPs could be observed to be surrounded by uncoated $CsPbBr_3$ NCs. TEM images with a higher magnification proved that the β-phase LnNP40 NPs with a size below 8 nm could be seeded to form heterostructure (Fig. 3c). The LnNPs with sizes above 8 nm had a close contact with the surface of $CsPbBr_3$ NCs or were partially coated without forming a core-shell structure (Fig. 3c). The selected area diffraction (SAD) pattern of LnNPs

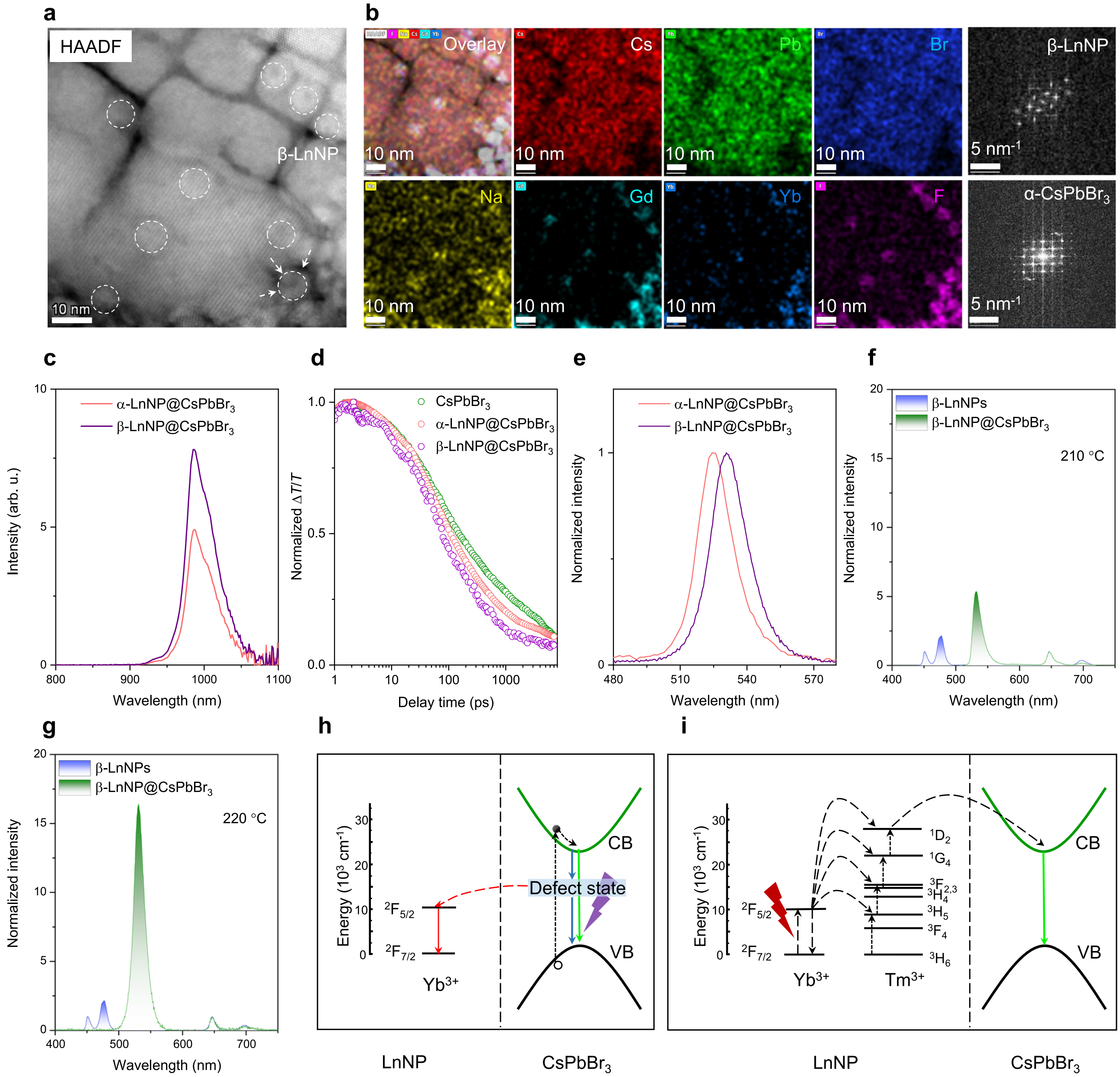

Fig. 2 | Two way energy transfer in optically active LnNP@CsPbBr$_3$ heterostructures. a HAADF-STEM image of β-LnNP@CsPbBr$_3$ heterostructures. **b** Corresponding EDS elemental mapping of these heterostructures and FFT images to show the phases. **c** NIR downconversion emission spectra of α/β-LnNP@CsPbBr$_3$ heterostructures under 365 nm laser excitation under the same measurement conditions (concentration of 50 mg mL^{-1}). **d** GSB kinetics of CsPbBr$_3$ NCs and α/β-LnNP@CsPbBr$_3$ heterostructures under 400 nm pump at a fluence of 23.1 μJ cm^{-2}. **e** Normalized upconversion emission spectra of α/β-LnNP@CsPbBr$_3$ heterostructures under 980 nm laser excitation. Comparison of upconversion emission spectra of β-LnNPs and β-LnNP@CsPbBr$_3$ heterostructures under 980 nm laser excitation (at a power density of 2 W cm^{-2}) with reaction temperature at **f** 210 and **g** 220 °C. Simplified two-way energy transfer pathways under **h** 365 and **i** 980 nm excitation. Source data are provided as a Source Data file.

showed a hexagonal diffraction pattern of the 8.57 nm LnNP. The SAD pattern of the selected LnNP@CsPbBr$_3$ heterostructure showed a clear combination pattern of hexagonal LnNP and cubic phase CsPbBr$_3$ NC. The TEM images also showed the change of preferable orientation from pure CsPbBr$_3$ NC with (110) and (002) to CsPbBr$_3$ shell in heterostructure with (020) and (200) (Fig. 3c). This also confirmed that seeding LnNP into CsPbBr$_3$ would change the crystal structure of CsPbBr$_3$ around core LnNP.

Larger LnNP60 and CSS NPs could not perform as a core to form heterostructure as only mixtures of LnNPs and CsPbBr$_3$ NCs could be observed in TEM images (Fig. 3e, g). To check the difference of energy transfer between heterostructure and mixture, we now check about the PL lifetimes of Yb^{3+} ions at 980 nm under the excitation of pulsed 930 nm flash lamp light (Fig. 3i). For mixtures of LnNP60 + CsPbBr$_3$ and CSS+CsPbBr$_3$, the lifetimes of Yb^{3+} ions obtained from time-correlated single-photon counting (TCSPC) measurements did not show a significant change by mixing LnNPs with CsPbBr$_3$ NCs, even shelled CSS showed a much longer lifetime of 553 μs than LnNP60 with a lifetime of 43 μs (Fig. 3i). However, LnNP@CsPbBr$_3$ heterostructures seeded by LnNP40 showed a decreased lifetime from 43 to 34 μs, indicating the direct LRET only happened within core-shell heterostructures, even only part of LnNP40 NPs could be seeded to form heterostructures. This is another strong evidence to prove that only smaller LnNPs could seed into CsPbBr$_3$ to form core-shell heterostructures and the size of core LnNPs is a crucial factor in the heterostructure formation. Due to the relative larger sizes and better crystallinity of LnNP40 and LnNP60

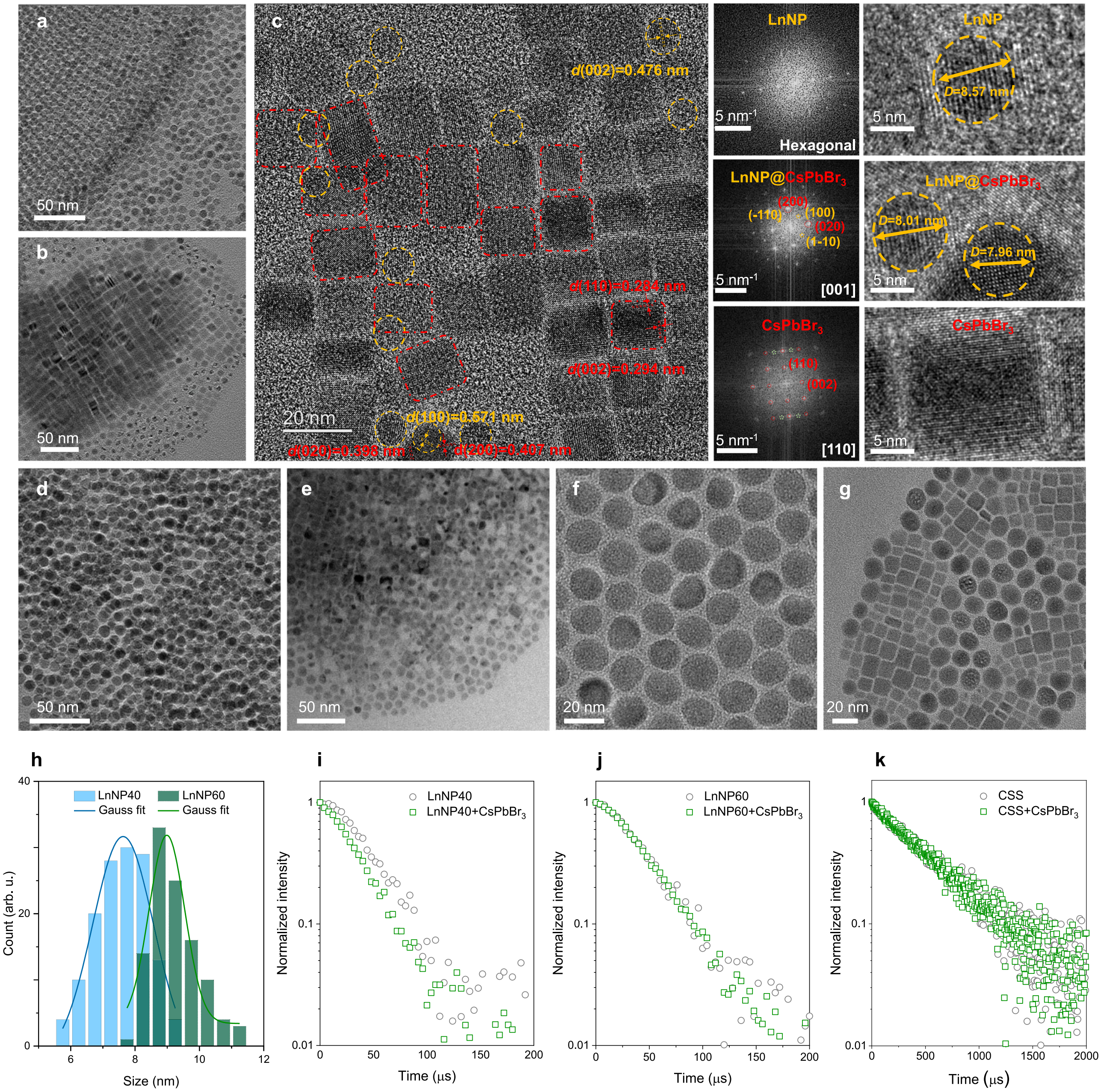

Fig. 3 | The size limit to form LnNP@CsPbBr$_3$ core-shell heterostructures. TEM images of **a** LnNP40, and **b** LnNP40 + CsPbBr$_3$. **c** TEM image of LnNP40 + CsPbBr$_3$ at higher magnification, corresponding selected area diffraction and HRTEM images of LnNP, LnNP@CsPbBr$_3$ heterostructure and CsPbBr$_3$ NC. TEM images of **d** LnNP60, **e** LnNP60 + CsPbBr$_3$, **f** CSS, and **g** CSS+CsPbBr$_3$. **h** Size distribution of LnNP40 and LnNP60. TCSPC measurements at 980 nm under 930 nm pump light excitation of **i** LnNP40 and LnNP40 + CsPbBr$_3$, **j** LnNP60 and LnNP60 + CsPbBr$_3$, **k** CSS and CSS+CsPbBr$_3$. Source data are provided as a Source Data file.

NPs, we can see a much clearer characteristic (100) peak from β-NaLnF$_4$ in LnNP40 + CsPbBr$_3$ and LnNP60 + CsPbBr$_3$ mixtures (Supplementary Fig. 14).

Through these experiments, we found that the seeding with larger LnNPs did not result in core-shell heterostructure formation, with the LHP NCs growing separately from the larger LnNP60 or CSS LnNPs. This proves our hypothesis that size is a key factor in LnNP@LHP core-shell heterostructure formation when LnNPs were used as seeds. We now can conclude that the size limit of LnNP cores to be encapsulated in CsPbBr$_3$ is 8 nm.

In conclusion, we have overcome a major bottleneck in the synthesis of heterostructures by resolving the critical issue of lattice mismatch using sub-8 nm LnNPs as seeds, leading to the fabrication of core-shell LnNP@LHP heterostructures. We further prove that core sizes below 8 nm along with a high reaction temperature is the determining factor rather than crystal phase mismatch between LHP and LnNP when forming LnNP@LHP core-shell heterostructures. CsPbBr$_3$ was grown onto both α and β-phase LnNPs, and β-LnNPs showed enhanced two-way energy transfer involving downconversion under 365 nm and upconversion 980 nm excitation. The direct coating of CsPbBr$_3$ onto LnNPs utilizes the advantage of LHP for high surface defect tolerance and demonstrates improved optical performance. The formation of LnNP@LHP heterostructures is rarely reported despite its potential in improving the performance and functionality of optoelectronic devices. We hope that this work has enabled a better understanding of how heterostructures can be more effectively synthesized, and will inspire further development of LnNP@LHP heterostructures as scintillators in X-ray detection, as well as light absorbers in highly efficient photovoltaic and anticounterfeiting applications.

Methods

Materials

Yttrium (III) acetate hydrate ($Y(CH_3COO)_3 \cdot xH_2O$, 99.9%), gadolinium acetate hydrate ($Gd(CH_3COO)_3 \cdot xH_2O$, 99.9%), ytterbium acetate hydrate ($Yb(CH_3COO)_3 \cdot xH_2O$, 99.9%), thulium acetate hydrate ($Tm(CH_3COO)_3 \cdot xH_2O$, 99.9%), cesium carbonate (Cs_2CO_3, 99.9%), lead chloride ($PbCl_2$, 99.999%), lead bromide ($PbBr_2$, 99.99%), lead iodide (PbI_2, 99.999%), 1-octadecene (ODE, 90%), oleic acid (OA, 90%), oleylamine (OAm, 70%) and *n*-hexane (HPLC grade) were purchased from Sigma-Aldrich and used directly without any further purification.

Synthesis of α-$NaYF_4$/α-$NaY_{0.69}F_4$:$Yb_{0.3}Tm_{0.01}$ LnNPs

All the LnNPs have been produced using a method from ref. 28 with modifications. $Y(CH_3COO)_3 \cdot xH_2O$, $Yb(CH_3COO)_3 \cdot xH_2O$ and $Tm(CH_3COO)_3 \cdot xH_2O$ with a total lanthanide amount of 1 mmol were added to a 50 mL flask containing oleic acid (3 mL) and 1-octadecene (7 mL). The resulting mixture is heated at 140 °C under argon flow for 1 h and cooled down to room temperature. Subsequently, a methanol solution (3 mL) containing NH_4F (0.48 mmol) and NaOH (0.3 mmol) was added and stirred at 70 °C for 45 min to remove the residual methanol from the reaction mixture. Upon removal of methanol, the solution was heated to 300 °C under a nitrogen flow and maintained at this temperature for 20 min. The solution was then cooled naturally to room temperature. The resulting LnNPs were precipitated out with an addition of ethanol, collected by 11617 × *g* centrifugation, and finally dispersed in 7 mL of hexane.

Synthesis of β-$NaGdF_4$/β-$NaGd_{0.69}F_4$:$Yb_{0.3}Tm_{0.01}$ LnNPs

$Gd(CH_3COO)_3 \cdot xH_2O$, $Yb(CH_3COO)_3 \cdot xH_2O$ and $Tm(CH_3COO)_3 \cdot xH_2O$ with a total lanthanide amount of 0.5 mmol were added to a 50 mL flask containing oleic acid (3 mL) and 1-octadecene (7 mL). The resulting mixture is heated at 140 °C under argon flow for 1 h and cooled down to room temperature. Subsequently, a methanol solution (6 mL) containing NH_4F (0.96 mmol) and NaOH (0.6 mmol) was added and stirred at 70 °C for 45 min to remove the residual methanol from the reaction mixture. Upon removal of methanol, the solution was heated to 300 °C under a nitrogen flow and maintained at this temperature for 20 min. The solution was then cooled naturally to room temperature. The resulting LnNPs were precipitated out with an addition of ethanol, collected by 11,617 × *g* centrifugation, and finally dispersed in 7 mL of hexane. LnNP40 and LnNP60 were synthesized using a similar method with prolonged reaction time to 40 and 60 min.

Synthesis of core LnNPs

$Gd(CH_3COO)_3 \cdot xH_2O$, $Yb(CH_3COO)_3 \cdot xH_2O$ and $Tm(CH_3COO)_3 \cdot xH_2O$ with a total lanthanide amount of 1 mmol were added to a 100 mL flask containing oleic acid (6 mL) and 1-octadecene (14 mL). The resulting mixture is heated at 140 °C under argon flow for 1 h and cooled down to room temperature. Subsequently, a methanol solution (6 mL) containing NH_4F (0.96 mmol) and NaOH (0.6 mmol) was added and stirred at 70 °C for 45 min under nitrogen flow to remove the residual methanol from the reaction mixture. Upon removal of methanol, the solution was heated to 300 °C under a nitrogen flow and maintained at this temperature for 60 min. The solution was then cooled naturally to room temperature. The resulting LnNPs were precipitated out with an addition of ethanol, collected by 7435 × *g* centrifugation, and finally dispersed in 7 mL of hexane.

Synthesis of core-shell LnNPs

$Gd(CH_3COO)_3 \cdot xH_2O$ and $Yb(CH_3COO)_3 \cdot xH_2O$ with a total lanthanide amount of 1 mmol were added to a 100 mL flask containing oleic acid (6 mL) and 1-octadecene (14 mL). The resulting mixture is heated at 140 °C under argon flow for 1 h and cooled down to room temperature. 3 mL of the as-synthesized $NaGd_{0.79}F_4$:$Yb_{0.2}$,$Tm_{0.01}$ core LnNPs were then added into the reaction flask. Subsequently, a methanol solution (5 mL) containing NH_4F (0.8 mmol) and NaOH (0.5 mmol) was added and stirred at 70 °C for 45 min under nitrogen flow to remove the residual methanol from the reaction mixture. Upon removal of methanol, the solution was heated to 300 °C under a nitrogen flow and maintained at this temperature for 45 min. The solution was then cooled naturally to room temperature. The resulting core-shell LnNPs were precipitated out with an addition of ethanol, collected by 7435 × *g* centrifugation, and finally dispersed in 7 mL of hexane.

Synthesis of CSS LnNPs

$Gd(CH_3COO)_3 \cdot xH_2O$ with a total lanthanide amount of 1 mmol were added to a 100 mL flask containing oleic acid (6 mL) and 1-octadecene (14 mL). The resulting mixture is heated at 140 °C under argon flow for 1 h and cooled down to room temperature. 3 mL of the as-synthesized $NaGd_{0.79}F_4$:$Yb_{0.2}$,$Tm_{0.01}$@$NaGd_{0.3}F_4$:$Yb_{0.7}$ core-shell LnNPs were then added into the reaction flask. Subsequently, a methanol solution (5 mL) containing NH_4F (0.8 mmol) and NaOH (0.5 mmol) was added and stirred at 70 °C for 45 min under nitrogen flow to remove the residual methanol from the reaction mixture. Upon removal of methanol, the solution was heated to 300 °C under a nitrogen flow and maintained at this temperature for 45 min. The solution was then cooled naturally to room temperature. The resulting CSS LnNPs were precipitated out with an addition of ethanol, collected by 7435 × *g* centrifugation, and finally dispersed in 7 mL of hexane.

Synthesis of Cs-oleate

Cs_2CO_3 (0.4 g), OA (1.25 mL) and ODE (15 mL) were added into a 50 mL three neck round-bottom flask. The reactants were stirred and heated to 150 °C under argon (Ar) flow for 1 h until fully dissolved. The flask is cooled down to 130 °C and maintained under Ar flow throughout the experiment.

Synthesis of $CsPbX_3$ NCs

For a typical reaction (0.5 mmol PbX_2), $PbCl_2$ (0.1391 g)/$PbBr_2$ (0.1835 g)/PbI_2 (0.2305 g), ODE (15 mL), OA (1.5 mL) and OAm (1.5 mL) were added into a 50 mL three neck round-bottom flask. The reactants were stirred and heated to 120 °C under nitrogen flow for 1 h until fully dissolved. The flask is then heated up to 180 °C. 1 mL of Cs-oleate is then injected into the reaction mixture. After 10 s, the flask is either placed in an ice-water bath, water bath or air cooled by lifting, with the heating mantle switched off. After cooling down to room temperature, the resulting NCs are precipitated out by centrifuge at 11,617 × *g* for 10 min. The precipitate is then dispersed in 7 mL of hexane, centrifuged to get rid of large NCs, and stored in a glass vial for future usage.

Synthesis of heterostructures

For LnNP seeded growth of heterostructures, the method is similar to the synthesis of $CsPbX_3$ NCs. Core LnNPs were washed for twice using ethanol before seeding the growth of LHP shell and filtered to ger rid of large LnNPs. 0.15 g of purified LnNPs in 1.5 mL hexane and 0.1835 g of $PbBr_2$ (0.5 mmol), along with ODE (15 mL), OA (1.5 mL) and OAm (1.5 mL) were added into the reaction flask before the stirring and heating step. The ratio of LnNP cores and $PbBr_2$ precursor can be tuned to manipulate the numbers of cores in heterostructures. The reactants were stirred and heated to 160 °C to get rid of hexane under nitrogen flow until fully dissolved. The flask is then heated up to 220 °C. We also note that the reaction temperature can be tuned, but maintaining a transparent precursor solution. The high reaction temperature at 220 °C will aid the growth of perovskite shells onto both α-LnNP and β-LnNP cores, even though β-LnNP cores have larger lattice constants, which will not lead to significant homogenous nucleation for both α- and β-LnNP cores. 1 mL of Cs-oleate is then swiftly injected into the reaction mixture. After 60 s, the flask is placed in water bath to cool down, with the heating mantle switched off. After cooling down to room temperature, the resulting heterostructures are precipitated out by centrifuge at 11,617 × *g* for 10 min. The precipitate is then dispersed in 7 mL of hexane, centrifuged to get rid of large aggregates, and stored in a glass vial for future usage.

Characterization

TEM, HRTEM, dark field-scanning TEM (DF-STEM), and EDS images were captured using a JEOL TEM-2100F transmission electron microscope operating at 200 kV. HAADF-STEM images were obtained on a FEI Tecnai Osiris 80-200 (S)TEM operated at 200 kV. The length of the NCs for all the samples were measured using ImageJ software. XRD was conducted with a D8 Advance Bruker X-ray diffractometer with Cu K_α radiation ($\lambda = 1.5406$ Å) from 10° to 80° with various counting time per step. UV-Vis absorption spectra were obtained using a Shimadzu UV2450/UV3600 spectrometer, by dispersing the samples in hexane at various concentrations in a standard quartz cuvette at room temperature. PL spectra in visible range were obtained using a Fluoromax-4, Horiba Jobin Yvon spectrofluorometer by dispersing the samples in hexane at various concentrations in a standard quartz cuvette at room temperature. PLQE measurements were carried out using a Spectralon coated integrating sphere. Measurements were taken at room temperature using CW laser diodes as the excitation source. Light from the experiment was collected using an optical fiber connected to an Andor Kymera 328i spectrometer housing a DU420A Silicon CCD detector. Setup calibration was performed using a Bentham 610 QTH calibration source. NIR emission spectra and TCSPC measurements were obtained on FLS1000 photoluminescence spectrometer from Edinburgh Instruments. The fitting of lifetime is based on Eqs. (1) and (2).

$$y = y_0 + A_1{*}e^{-(x-x_0)/t_1} + A_2{*}e^{-(x-x_0)/t_2} \tag{1}$$

$$\tau_{\text{average}} = (A_1{*}t_1{}^2 + A_2{*}t_2{}^2)/(A_1{*}t_1 + A_2{*}t_2) \tag{2}$$

Intensity calculation in HAADF image

The heterostructure samples were observed using a FEI Tecnai Osiris 80-200 (S)TEM operated at 200 kV. To minimize beam damage, HAADF-STEM images were acquired using a beam current of around 140 pA, 30 ms per pixel dwell time, camera length of 115 mm. HAADF image contrast is related to the elastic scattering of electrons in the sample. The detailed calculation has been listed in Supplementary Information.

Transient absorption spectroscopy

Transient absorption measurements are performed using HARPIA transient absorption system (Light Conversion) at room temperature. The fundamental laser (PHAROS, Light Conversion, 1030 nm, 10 kHz) was divided into two beams for the generation of pump and probe beam respectively. The pump beam was generated by collinear optical parametric amplifier (ORPHEUS, Light Conversion). The probe beam was obtained by focusing 1030 nm laser on a sapphire crystal. The pump beam overlapped with the probe beam at the sample. The polarization of pump beam was set to magic angle (54.7°) relative to probe beam. The average lifetime obtained by TA is calculated based on Eqs. (3)–(6).

$$y = y_0 + A_1{*}e^{-(x-x_0)/t_1} + A_2{*}e^{-(x-x_0)/t_2} \tag{3}$$

$$\tau_{\text{average}} = (A_1{*}t_1{}^2 + A_2{*}t_2{}^2)/(A_1{*}t_1 + A_2{*}t_2) \tag{4}$$

or

$$y = y_0 + A_1{*}e^{-(x-x_0)/t_1} + A_2{*}e^{-(x-x_0)/t_2} + A_3{*}e^{-(x-x_0)/t_3} \tag{5}$$

$$\tau_{\text{average}} = (A_1{*}t_1{}^2 + A_2{*}t_2{}^2 + A_3{*}t_3{}^2)/(A_1{*}t_1 + A_2{*}t_2 + A_3{*}t_3) \tag{6}$$

Data availability

The data that support the findings of this study are available from the corresponding authors upon request. Source data are provided with this paper.

References

1. Ollearo, R. et al. Ultralow dark current in near-infrared perovskite photodiodes by reducing charge injection and interfacial charge generation. *Nat. Commun.* **12**, 7277 (2021).
2. Min, H. et al. Perovskite solar cells with atomically coherent interlayers on SnO_2 electrodes. *Nature* **598**, 444–450 (2021).
3. Lin, R. et al. Monolithic all-perovskite tandem solar cells with 24.8% efficiency exploiting comproportionation to suppress Sn(ii) oxidation in precursor ink. *Nat. Energy* **4**, 864–873 (2019).
4. Jena, A. K., Kulkarni, A. & Miyasaka, T. Halide Perovskite Photovoltaics: Background, Status, and Future Prospects. *Chem. Rev.* **119**, 3036–3103 (2019).
5. Wang, L. et al. A Eu^{3+}-Eu^{2+} ion redox shuttle imparts operational durability to Pb-I perovskite solar cells. *Science* **363**, 265–270 (2019).
6. Pan, G. et al. Doping Lanthanide into Perovskite Nanocrystals: Highly Improved and Expanded Optical Properties. *Nano Lett.* **17**, 8005–8011 (2017).
7. Zhou, D. et al. Impact of Host Composition, Codoping, or Tridoping on Quantum-Cutting Emission of Ytterbium in Halide Perovskite Quantum Dots and Solar Cell Applications. *Nano Lett.* **19**, 6904–6913 (2019).
8. Zeng, Z. et al. Multimodal Luminescent $Yb^{3+}/Er^{3+}/Bi^{3+}$ -Doped Perovskite Single Crystals for X-ray Detection and Anti-Counterfeiting. *Adv. Mater.* **32**, e2004506 (2020).
9. Duan, J. et al. Lanthanide Ions Doped $CsPbBr_3$ Halides for HTM-Free 10.14%-Efficiency Inorganic Perovskite Solar Cell with an Ultrahigh Open-Circuit Voltage of 1.594 V. *Adv. Energy Mater.* **8**, 1802346 (2018).
10. Song, Z. et al. Incorporating of Lanthanides Ions into Perovskite Film for Efficient and Stable Perovskite Solar Cells. *Small* **16**, e2001770 (2020).
11. Kojima, A., Teshima, K., Shirai, Y. & Miyasaka, T. Organometal halide perovskites as visible-light sensitizers for photovoltaic cells. *J. Am. Chem. Soc.* **131**, 6050–6051 (2009).
12. Yu, Z., Chan, W. K. & Tan, T. T. Y. Neodymium-Sensitized Nanoconstructs for Near-Infrared Enabled Photomedicine. *Small* **16**, 1905265 (2020).
13. Tew, A. et al. Heterostructures enhance the absorption of lanthanides. *Appl. Phys. Rev.* **11**, 021329 (2024).

14. Heliotis, G. et al. Hybrid Inorganic/Organic Semiconductor Heterostructures with Efficient Non-Radiative Energy Transfer. *Adv. Mater.* **18**, 334–338 (2006).
15. Ruan, L. & Zhang, Y. NIR-excitable heterostructured upconversion perovskite nanodots with improved stability. *Nat. Commun.* **12**, 219 (2021).
16. Xiao, H. et al. Core-Shell Structured Upconversion/Lead-Free Perovskite Nanoparticles for Anticounterfeiting Applications. *Angew. Chem. Int. Ed.* **61**, e202115136 (2022).
17. Liu, J. & Zhang, J. Nanointerface Chemistry: Lattice-Mismatch-Directed Synthesis and Application of Hybrid Nanocrystals. *Chem. Rev.* **120**, 2123–2170 (2020).
18. Ning, Z. et al. Quantum-dot-in-perovskite solids. *Nature* **523**, 324–328 (2015).
19. Li, H. et al. Realization of 1.54-microm Light-Emitting Diodes Based on Er^{3+} /Yb^{3+} Co-Doped $CsPbCl_3$ Films. *Adv. Mater.* **35**, e2300118 (2023).
20. Milstein, T. J., Kroupa, D. M. & Gamelin, D. R. Picosecond Quantum Cutting Generates Photoluminescence Quantum Yields Over 100% in Ytterbium-Doped $CsPbCl_3$ Nanocrystals. *Nano Lett.* **18**, 3792–3799 (2018).
21. Ye, J. et al. Extending the defect tolerance of halide perovskite nanocrystals to hot carrier cooling dynamics. *Nat. Commun.* **15**, 8120 (2024).
22. Guo, Q. et al. High performance perovskite solar cells based on β-$NaYF_4$:Yb^{3+}/Er^{3+}/Sc^{3+}@$NaYF_4$ core-shell upconversion nanoparticles. *J. Power Sources* **426**, 178–187 (2019).
23. Francés-Soriano, L. et al. Efficient Cementing of $CH_3NH_3PbBr_3$Nanoparticles to Upconversion Nanoparticles Visualized by Confocal Microscopy. *Adv. Funct. Mater.* **26**, 5131–5138 (2016).
24. Estebanez, N. et al. Linear Coassembly of Upconversion and Perovskite Nanoparticles: Sensitized Upconversion Emission of Perovskites by Lanthanide-Doped Nanoparticles. *Adv. Funct. Mater.* **30**, 2003766 (2020).
25. Xie, L. et al. Broadband Detection of X-ray, Ultraviolet, and Near-Infrared Photons using Solution-Processed Perovskite-Lanthanide Nanotransducers. *Adv. Mater.* **33**, e2101852 (2021).
26. Cherniukh, I. et al. Perovskite-type superlattices from lead halide perovskite nanocubes. *Nature* **593**, 535–542 (2021).
27. Zhang, Y. et al. Ultrasmall-Superbright Neodymium-Upconversion Nanoparticles via Energy Migration Manipulation and Lattice Modification: 808 nm-Activated Drug Release. *ACS Nano* **11**, 2846–2857 (2017).
28. Yu, Z. et al. Balancing the thickness of sensitizing and inert layers in neodymium-sensitized tetralayer nanoconstructs for optimal ultraviolet upconversion and near-infrared cross-linked hydrogel tissue sealants. *Biomater. Sci.* **8**, 2878–2886 (2020).
29. Yang, Y. et al. Ultra-small bimetallic iron–palladium (FePd) nanoparticle loaded macrophages for targeted tumor photothermal therapy in NIR-II biowindows and magnetic resonance imaging. *RSC Adv.* **9**, 33378–33387 (2019).
30. Travis, W., Glover, E. N. K., Bronstein, H., Scanlon, D. O. & Palgrave, R. G. On the application of the tolerance factor to inorganic and hybrid halide perovskites: a revised system. *Chem. Sci.* **7**, 4548–4556 (2016).
31. Chen, J. et al. Molecule-induced ripening control in perovskite quantum dots for efficient and stable light-emitting diodes. *Sci. Adv.* **11**, eads7159 (2025).
32. Protesescu, L. et al. Nanocrystals of Cesium Lead Halide Perovskites ($CsPbX_3$, X = Cl, Br, and I): Novel Optoelectronic Materials Showing Bright Emission with Wide Color Gamut. *Nano Lett.* **15**, 3692–3696 (2015).
33. Chen, Y. et al. Hybrid Field-Effect Transistors and Photodetectors Based on Organic Semiconductor and $CsPbI_3$ Perovskite Nanorods Bilayer Structure. *Nanomicro Lett.* **10**, 57 (2018).
34. Zhang, J.-Y., Wang, X.-Y., Xiao, M., Qu, L. & Peng, X. Lattice contraction in free-standing CdSe nanocrystals. *Appl. Phys. Lett.* **81**, 2076–2078 (2002).
35. Chen, X., Samia, A. C. S., Lou, Y. & Burda, C. Investigation of the Crystallization Process in 2 nm CdSe Quantum Dots. *J. Am. Chem. Soc.* **127**, 4372–4375 (2005).
36. Wang, Y., Yang, Y., Wang, P. & Bai, X. Concentration- and temperature-dependent photoluminescence of $CsPbBr_3$ perovskite quantum dots. *Optik* **139**, 56–60 (2017).
37. Raino, G. et al. Superfluorescence from lead halide perovskite quantum dot superlattices. *Nature* **563**, 671–675 (2018).
38. Tong, Y. et al. Spontaneous Self-Assembly of Perovskite Nanocrystals into Electronically Coupled Supercrystals: Toward Filling the Green Gap. *Adv. Mater.* **30**, 1801117 (2018).
39. Huang, H. et al. Growth of Perovskite $CsPbBr_3$ Nanocrystals and Their Formed Superstructures Revealed by In Situ Spectroscopy. *Chem. Mater.* **32**, 8877–8884 (2020).
40. Chan, W. K., Zhou, D., Yu, Z. & Tan, T. T. Y. Mechanistic studies of $CsPbBr_3$ superstructure formation. *J. Mater. Chem. C.* **9**, 14699–14708 (2021).
41. Gan, Z. et al. The Dominant Energy Transport Pathway in Halide Perovskites: Photon Recycling or Carrier Diffusion? *Adv. Energy Mater.* **9**, 1900185 (2019).
42. Chan, W. K. et al. Hybrid Organic-Inorganic Perovskite Superstructures for Ultrapure Green Emissions. *Nanomaterials* **13**, 815 (2023).
43. Rossi, D., Parobek, D., Dong, Y. & Son, D. H. Dynamics of Exciton–Mn Energy Transfer in Mn-Doped $CsPbCl_3$ Perovskite Nanocrystals. *J. Phys. Chem. C.* **121**, 17143–17149 (2017).
44. Butkus, J. et al. The Evolution of Quantum Confinement in $CsPbBr_3$ Perovskite Nanocrystals. *Chem. Mater.* **29**, 3644–3652 (2017).
45. Wang, J., Cheng, C. & De, G. Crystallinity effects and phase transition on upconversion emission of monodisperse $NaGdF_4$:Yb, Er nanocrystals. *Optical Mater.* **91**, 419–424 (2019).
46. Egerton, R. F. Electron energy-loss spectroscopy in the TEM. *Rep. Prog. Phys.* **72**, 016502 (2009).
47. Gong, K. & Kelley, D. F. Lattice Strain Limit for Uniform Shell Deposition in Zincblende CdSe/CdS Quantum Dots. *J. Phys. Chem. Lett.* **6**, 1559–1562 (2015).
48. Shan, Z. W. et al. Ultrahigh stress and strain in hierarchically structured hollow nanoparticles. *Nat. Mater.* **7**, 947–952 (2008).
49. Smith, A. M., Mohs, A. M. & Nie, S. Tuning the optical and electronic properties of colloidal nanocrystals by lattice strain. *Nat. Nanotechnol.* **4**, 56–63 (2009).
50. Yang, S., Prendergast, D. & Neaton, J. B. Strain-induced band gap modification in coherent core/shell nanostructures. *Nano Lett.* **10**, 3156–3162 (2010).
51. Zhao, Q. et al. Controlling structural symmetry of a hybrid nanostructure and its effect on efficient photocatalytic hydrogen evolution. *Adv. Mater.* **26**, 1387–1392 (2014).
52. Yi, G. S. & Chow, G. M. Synthesis of Hexagonal-Phase $NaYF_4$:Yb,Er and $NaYF_4$:Yb,Tm Nanocrystals with Efficient Up-Conversion Fluorescence. *Adv. Funct. Mater.* **16**, 2324–2329 (2006).
53. Wang, F., Wang, J. & Liu, X. Direct evidence of a surface quenching effect on size-dependent luminescence of upconversion nanoparticles. *Angew. Chem. Int. Ed.* **49**, 7456–7460 (2010).
54. Liu, Q. et al. Sub-10 nm hexagonal lanthanide-doped $NaLuF_4$ upconversion nanocrystals for sensitive bioimaging in vivo. *J. Am. Chem. Soc.* **133**, 17122–17125 (2011).

55. Chen, G. et al. Lanthanide-doped ultrasmall yttrium fluoride nanoparticles with enhanced multicolor upconversion photoluminescence. *J. Mater. Chem*. **22**, 20190–20196 (2012).
56. van Turnhout, L. et al. Distance-Independent Efficiency of Triplet Energy Transfer from pi-Conjugated Organic Ligands to Lanthanide-Doped Nanoparticles. *J. Am. Chem. Soc.* **146**, 22612–22621 (2024).

Acknowledgements

This work was supported by the Ministry of Education of Singapore Tier 1 (RG128/19 (S)) and Tier 3 grant (MOE 2016 T3-1-004). TEM characterization was performed with support from the NTU Facility for analysis, testing, characterization, and simulation. B.X. thanks the Cambridge Trust, the China Scholarship Council and the Winton Programme for the Physics of Sustainability for funding. A.T. acknowledges support from the UKRI NanoDTC Cambridge EP/S022953/1.

Author contributions

Z.Y. conceived the project. Z.Y., W.K.C. and Z.J. performed the sample synthesis and characterization. Z.Y., A.R. and T.T.Y.T. supervised the project. D.Z. contributed to the synthesis of perovskite nanocrystals and provided advice for the synthesis of heterostructures. X.L. performed HAADF-STEM measurement and under the supervision of C.D. B.X., J.Y. and L.D. performed TA measurements. A.T. and L.v.T. performed TCSPC measurements. Y. L. Q.G. and T.L. performed XRD measurement. H.T.Z.Z. performed PL and stability measurements. S.D. performed PLQE measurements. Z.Y., W.K.C. and T.T.Y.T. wrote the paper with input from all authors.

Competing interests

The authors declare no competing interests.

Additional information

Supplementary information The online version contains supplementary material available at https://doi.org/10.1038/s41467-025-59315-y.

Correspondence and requests for materials should be addressed to Zhongzheng Yu or Timothy Thatt Yang Tan.

Peer review information *Nature Communications* thanks the anonymous reviewers for their contribution to the peer review of this work. A peer review file is available.